

Running title: Representations of adversarial images in DNNs and the human brain

Dissociable neural representations of adversarially perturbed images in deep neural networks and the human brain

Chi Zhang¹, Xiaohan Duan¹, Linyuan Wang¹, Yongli Li², Bin Yan¹, Guoen Hu¹, Ruyuan
Zhang^{3*}, Li Tong^{1*}

¹National Digital Switching System Engineering and Technological Research Center,
Zhengzhou, China, 450000

² People's Hospital of Henan Province, Zhengzhou, China, 450000

³Center for Magnetic Resonance Imaging, Department of Neuroscience, University of
Minnesota at Twin Cities, MN. USA. 55108

* co-senior authors

Correspondence:

Ruyuan Zhang
Center for Magnetic Resonance Research
University of Minnesota
2021 6h St SE
Minneapolis, MN 55455-3007
585-752-6673
zhan1217@umn.edu

Li Tong
National Digital Switching System Engineering and Technological Research Center
No.7, Jianxue Street, Wenhua Road
Zhengzhou City, China, 450000
0086-0371-5598080
tttocean@163.com

ABSTRACT

Despite the remarkable similarities between deep neural networks (DNN) and the human brain as shown in previous studies, the fact that DNNs still fall behind humans in many visual tasks suggests that considerable differences still exist between the two systems. To probe their dissimilarities, we leverage adversarial noise (AN) and adversarial interference (AI) images that yield distinct recognition performance in a prototypical DNN—AlexNet and human vision. The evoked activity by regular (RE) and adversarial images in both systems is thoroughly compared. We find that representational similarity between RE and adversarial images in the human brain resembles their perceptual similarity. However, such representation-perception association is disrupted in the DNN. Especially, the representational similarity between RE and AN images idiosyncratically increases from low- to high-level layers. Furthermore, forward encoding modeling reveals that the DNN-brain hierarchical correspondence proposed in previous studies only holds when the two systems process RE and AI images but not AN images. These results might be due to the deterministic modeling approach of current DNNs. Taken together, our results provide a complementary perspective on the comparison between DNNs and the human brain, and highlight the need to characterize their differences to further bridge artificial and human intelligence research.

Keywords: adversarial images, deep neural network, human visual cortex, functional magnetic resonance imaging, representational similarity analysis, forward encoding model.

INTRODUCTION

Past a few years have seen remarkable advances in applications of deep neural networks (DNNs) in a variety of computer vision tasks ([LeCun Y et al. 2015](#)). These dazzling achievements of DNNs also inspire neuroscientists to consider using it as a ubiquitous computational framework to understand the mechanisms of biological vision ([Jozwik KM et al. 2016](#); [Yamins DLK and JJ DiCarlo 2016](#)). Indeed, even from as early as the birth, the design of neural networks bore strong resemblances to the structures and functions of the mammalian visual system. For example, most DNNs encompass several convolutional layers that aim to extract local visual statistics, a form of computation that is similar to the receptive field structure of cortical neurons ([LeCun Y and Y Bengio 1998](#)). In addition, the hierarchical design of DNNs is also consonant with the processing hierarchy along the ventral pathway in the brain ([Krizhevsky A et al. 2012](#)). These qualitative similarities have been recently extended to quantitative correspondences—visual features in different layers of DNNs can accurately predict spatiotemporal characteristics of brain signals ([Agrawal P et al. 2014](#); [Yamins DL et al. 2014](#); [Guclu U and MA van Gerven 2015](#); [Cichy RM et al. 2016](#); [Hong H et al. 2016](#); [Guclu U and MAJ van Gerven 2017](#); [Horikawa T and Y Kamitani 2017](#); [Khaligh-Razavi S-M et al. 2017](#)). In sum, existing evidence demonstrates that modern DNNs share many key features with biological visual systems in terms of visual processing.

Despite the tremendous success of DNNs in computer vision tasks, current DNNs still considerably fall behind human vision in many aspects, implying that fundamental differences still exist between the two systems. One potent example is the adversarially perturbed images, which can successfully “fool” even the most state-of-the-art DNNs

([Szegedy C et al. 2013](#); [Nguyen A et al. 2015](#)). Adversarial noise (AN) images look like meaningless noise to humans (Fig. 1B). DNNs, however, can classify them into object categories with surprisingly high confidence ([Nguyen A et al. 2015](#)). By contrast, humans can easily recognize adversarial interference (AI) images (Fig. 1C), which can be generated by deliberately adding a small amount of special noise to the regular (RE) images. However, the special noise severely impairs DNNs' recognition performance ([Szegedy C et al. 2013](#)). Adversarial images present a compelling example of double-dissociation between DNNs and the human brain, as the same input images produce drastically distinct perceptual outcomes in the two visual systems.

Adversarial images suggest one important defect of current DNNs—most DNNs are merely trained to match human behavioral performance but not explicitly trained to match neural representations in the human brain. Although several studies have shown that some performance-optimized DNNs also exhibit similarities to the neural processing in the human brain, the majority of these studies, however, employed the stimuli that can be easily recognized by both systems ([Guclu U and MA van Gerven 2015](#); [Guclu U and MAJ van Gerven 2017](#)). Especially, in those studies the same image input usually yields the same perceptual output from both systems. It is thus not surprising that the measured internal neural representations in the two systems are also comparable. Here, we argue that only by using the stimuli that create dissociable percepts, we can test the robustness of these similarities and gain further insight into in what aspect the two systems differ. To this end, adversarial images can be a good candidate to help delineate the representational difference between DNNs and human vision.

In the present study, we aimed to use adversarial images to characterize similarities and dissimilarities in the neural representation between AlexNet, a well-established DNN, and human vision. For the DNN, we compared how artificial neurons in different layers respond to RE images and their corresponding adversarial images, respectively. We also used functional magnetic resonance imaging (fMRI) to measure the neural response evoked by the RE and adversarial images in human participants. Using the representational similarity analysis (RSA) and forward encoding modeling, we were able to directly contrast the representational geometry within and across systems in order to understand the extent and limit of both systems.

MATERIALS AND METHODS

Ethics statement. All experimental protocols were approved by the Ethics Committee of the Henan Provincial People's Hospital. All research was performed in accordance with relevant guidelines and regulations. Informed written consent was obtained from all participants.

Subjects. Three healthy volunteers (one female and two males, aged 22~28 years) participated in the study. The subject S3 was the author C.Z. The other two subjects were naïve to the purpose of this study. All subjects were monolingual native-Chinese speakers, right-handed, and had normal or corrected-to-normal vision and considerable experience of fMRI experiments.

Convolutional Neural Network. We chose the well-established DNN architecture—AlexNet

and implemented it using the Caffe deep learning framework ([Krizhevsky A et al. 2012](#)). Briefly, AlexNet has been trained on the ImageNet database ([Deng J et al. 2009](#)) to classify an image into one of 1000 categories. AlexNet consists of eight layers: five convolutional layers at low-level processing stages and three fully-connected layers at higher-level processing stages (Fig. 1D). Each of the five convolutional layers includes 96, 256, 384, 384, and 256 linear convolutional kernels. Each of the three fully-connected layers consists of 4096, 4096 and 1000 artificial neurons. Each convolutional layer performs linear convolution and Rectified Linear Unit (ReLU) gating. Spatial max pooling is performed in layers 1, 2, and 5 to implement nonlinear downsampling that promotes invariances to small translations of visual input. Layers 1 and 2 additionally use the local response normalization to implement a competitive mechanism for local neuronal activity. The ReLU activation function and the dropout method are used in layers 6 and 7. Layer 8 uses the softmax function to output a vector of probabilities for an input image being classified into 1000 categories. In our study, each image was unified as a 227×227 matrix for each of three RGB color channels.

Image stimuli

Regular images. Regular (RE) images in our study were sampled from the ImageNet database ([Deng J et al. 2009](#)). ImageNet is currently the most advanced benchmark database on which almost all state-of-the-art DNNs are trained for image classification. We selected one image (width and height > 227 pixels and aspect ratio $> 2/3$ and < 1.5) from each of 40 representative object categories and AlexNet can classify them into correct categories with probabilities greater than 0.99. The 40 images can be evenly divided into 5 broad classes: dog,

bird, car, fruit, and aquatic animals.

Adversarial images. Adversarial images included adversarial noise (AN) images (Fig. 1B) and adversarial interference (AI) images (Fig. 1C). A pair of AN and AI images were generated with respect to each RE image, resulting in a total of 120 different pictures (40 RE + 40 AN + 40 AI) in the entire experiment.

The method to generate a corresponding AN image given a RE image has been documented in Nguyen A et al. ([Nguyen A et al. 2015](#)). We briefly summarized the method here. We initialized an AN image from the averaged image of all images in ImageNet. A small amount of Gaussian noise was added to this averaged image to break the symmetry. Given that the category of the corresponding RE image was known, and the DNN was already trained, we first forwardly computed the final probability of the corresponding category given the input image. This probability was expected to be initially low, and we used backpropagation to transduce the error signal from top to bottom layers until the image pixel space. The pixel values in the input image were then adjusted following the gradient to enhance the classification probability. We also included an additional regularization item to penalize the overall intensity of the image. Formally, let $P_c(I)$ be the probability of the class c given an image I . We would like to find an L_2 -regularized image I^* , such that it maximizes the following objective:

$$I^* = \arg \max_I P_c(I) - \lambda \|I - I_{mean}\|_2^2, \quad (1)$$

where λ is the regularization parameter and I_{mean} is the grand average of all images in ImageNet. This process was iterated until the output probability for the corresponding category reached 0.99. Note that the internal structure (i.e., all connection weights) of the

DNN was fixed throughout the entire training process and we only adjusted the pixel values of the input image.

AI images were generated using the similar approach. The optimization started from the corresponding RE image, and we adjusted the pixel values to enhance the probability of this image being classified into another broad class. All AI images were classified into a “wrong” class with a probability greater than 0.5. Choosing a lower probability for AI images avoids overly adding image noise and maximally preserve the similarity between RE and AI images. We further generated another set of AI images that reached 0.99 probability of “wrong” class and confirmed that results did not substantially change under this regime (see Fig. S1).

Apparatus. Stimuli were presented using a Sinorad LCD projector (resolution 1920×1080 at 120 Hz; size 89 cm \times 50 cm; viewing distance 168 cm) onto a rear-projection monitor located over the head of the subject. Subjects viewed the monitor via a mirror mounted on the head coil. All computer-controlled stimuli were programmed using Eprime 2.0. Behavioral responses were recorded using a button box.

fMRI experiments

Main experiment. Each subject completed two scanning sessions in the main experiment. Each session included five runs. In each session, a half of all the images (20 images \times 3 RE/AN/AI = 60 images) were presented. A scanning run contained 129 stimulus trials, with 2 trials per image and additional 9 blank trials. The presentation order of the images was

randomized within a run. In a trial, a blank lasted 2 s and was followed by a 2 s presentation of one image ($12^\circ \times 12^\circ$). A 20 s blank period was added to the beginning and end of each run to establish a good baseline and compensate the initial insatiability of the magnetic field. A fixation point ($0.2^\circ \times 0.2^\circ$) was shown at center-of-gaze throughout the entire run. Participants were instructed to maintain steady fixation throughout the entire run and press buttons to perform an animal judgment task—whether the image belongs to animals. The task aimed to engage subjects’ attention onto the stimuli.

Retinotopic mapping experiment. A retinotopic mapping experiment was performed to define early visual areas. The retinotopic experiment used standard rotating wedges and expanding rings consisting of textures of objects, faces, and words placed on an achromatic pink-noise background (<http://kendrickkay.net/analyzePRF/>). Early visual areas (V1–V4) were defined on the spherical cortical surfaces of individual subjects.

Functional localizer experiments. Two functional localizer experiments were conducted to locate lateral occipital (LO) cortex and human middle temporal (hMT+) lobe in each participant. Each localizer experiment included two runs. Both localizer experiments were aimed to create a more precise LO mask (see region-of-interests (ROI) definition section below).

In the LO localizer experiment, each run consisted of 16 stimulus blocks and 5 blank blocks. Each run began with a blank block, and a blank block was repeated after every 4 stimulus blocks. Each block lasted 16s. Intact images and their corresponding scrambled images were alternating in a stimulus block. Each stimulus block included 40 images (i.e., 20 intact + 20 scramble images). Each image ($12^\circ \times 12^\circ$) lasted 0.3 s and was followed by a

0.5 s blank.

In the hMT+ localizer experiment, each run consisted of 10 stimulus blocks. Within a 32 s stimulus block, a 24 s static dot stimulus and an 8 s moving-dot stimulus were alternately presented. Each stimulus subtended a $12^\circ \times 12^\circ$ square area at the center of the black background screen. An 8 s blank was added to the beginning and end of each run.

MRI data acquisition. All MRI data were collected using 3.0-Tesla Siemens MAGNETOM Prisma scanner and a 32-channel head coil at the Department of Radiology at the People's Hospital of Henan Province.

An interleaved T2*-weighted, single-shot, gradient-echo echo-planar imaging (EPI) sequence was used to acquire functional data (60 slices, slice thickness 2 mm, slice gap 0 mm, field of view $192 \times 192 \text{ mm}^2$, phase-encode direction anterior-posterior, matrix size 96×96 , TR 2 s, TE 29 ms, flip angle 76° , nominal spatial resolution $2 \times 2 \times 2 \text{ mm}^3$). Three B0 fieldmaps were acquired to aid post-hoc correction of EPI spatial distortion in each session (resolution $2 \times 2 \times 2 \text{ mm}^3$, TE_1 4.92 ms, TE_2 7.38 ms, TA 2.2 min). In addition, high-resolution T1-weighted anatomical (MPRAGE) images of the entire head were also acquired (TR 2300 ms, TE 2.26 ms, TI 900 ms, flip angle 8° , field of view $256 \times 256 \text{ mm}^2$, voxel size $1.0 \times 1.0 \times 1.0 \text{ mm}^3$).

MRI data preprocessing. The pial and the white surfaces for each subject were constructed using FreeSurfer (<http://surfer.nmr.mgh.harvard.edu>). An intermediate gray matter surface was also created between the pial and the white surfaces of each subject.

For functional data, we discarded the first 18, 14, and 6 s time series in the main experiment, the LO localizer experiment, and the MT localizer experiment respectively. Functional data then underwent slice time correction using cubic interpolation. The regularized time-interpolated fieldmaps were used to correct EPI spatial distortion. Rigid-body motion parameters were then estimated from the undistorted EPI volumes. Finally, the effect of distortion correction, head motion correction and data mapping from volumes to surfaces were concatenated and performed using a single interpolation step to maximally preserve spatial resolution.

General linear modeling. For the main experiment, we estimated the vertex responses (i.e., beta estimates from GLM modeling) of all stimulus trials using the GLMdenoise method ([Kay KN et al. 2013](#)). All blank trials were modeled as a single predictor. This analysis yielded beta estimations of 241 conditions (120 images \times 2 trials + 1 blank). Notably, we treated two presentations of the same image as distinct conditions in order to calculate the correlation of response patterns across trials evoked by the same image.

Region-of-interest (ROI) definitions. Based on the retinotopic experiment, we calculated the population receptive field (pRF) (<http://kendrickkay.net/analyzePRF>) of each vertex and defined low-level visual areas (V1–V4) based on the pRF map. To define LO, we first selected vertices showing significantly higher responses to the intact images than the scrambled images (two-tails t-test, $p < 0.05$, uncorrected). In addition, hMT+ was defined as the area showing significantly higher responses to the moving than the static dots (two-tails

t-test, $P < 0.05$, uncorrected). The intersection vertices between LO and hMT+ were then removed from LO. All visual areas were defined on the spherical cortical surfaces created by FreeSurfer (see Fig. 2A).

Vertex selection. In order to further select task related vertices in each ROI, we performed a searchlight analysis on flattened 2D cortical surfaces ([Chen Y et al. 2011](#)). For each vertex, we defined a 2D searchlight disk with 3 mm radius. The geodesic distance between two vertices was approximated by the length of the shortest path between them on the flattened surface. Using the vertices in the disk, we calculated two representational dissimilarity matrices (RDMs) of all RE images at the first and the second trials. Two RDMs were then compared (Spearman's R) to show the consistency of activity pattern across two trials. The 200/400 vertices (100/200 vertices from each hemisphere) with the highest correlation values across trials were selected in each ROI for further analysis. Note that vertex selection was only based on the responses to the RE images and did not involve any data for AN and AI images.

Representational similarity analysis. Representational similarity analysis (RSA) is a powerful method to characterize the representational geometry underlying many features ([Kriegeskorte N et al. 2008](#); [Kriegeskorte N and RA Kievit 2013](#)). Here, we seek to understand how RE and adversarial images are represented in the DNN and the brain. We applied RSA separately to the activity of the units in the DNN and the responses of the vertices in the brain.

RSA on DNN layers and brain ROIs. For one DNN layer, we computed the dissimilarity of unit activity between every pair of RE images. This computation yielded a 40×40 RDM for the RE images. Similarly, we obtained another two RDMs for the AN and AI images. We then calculated the representational similarity between these RDMs using the equations as follows:

$$R_{RE-AN} = corr(RDM_{RE}, RDM_{AN}), \quad (2)$$

$$R_{RE-AI} = corr(RDM_{RE}, RDM_{AI}), \quad (3)$$

where RDM_{RE} , RDM_{AN} and RDM_{AI} indicate the RDM of the RE, AN or AI images, respectively. This calculation generated one RE-AN similarity value and one RE-AI similarity value for each DNN layer (see Fig. 2B). We repeated the same analysis above on the human brain except that we used the activity of the vertices in a brain ROI.

To examine whether the RE-AN or the RE-AI similarity values significantly deviated from the null hypotheses, we randomized the image labels with respect to the endowed activity 1000 times and in each randomized sample recalculated the RE-AN and the RE-AI similarity values in one brain ROI or one DNN layer. This calculation produced two null hypothesis distributions for the two similarity values. The mean RE-AN or RE-AI similarity values (see below) were then tested against the null similarity distributions.

To examine the difference between the RE-AI and RE-AN similarity values, we resampled 80% units 1000 times without replacement and in each randomized sample recalculated the two similarity values in one brain ROI or one DNN layer. This analysis yielded a RE-AI similarity distribution (i.e., 1000 bootstrap samples) and a RE-AN similarity distribution. Two distributions gave the range of the 95% confidence interval (the error bars

in Figs. 3 and 5). The bootstrapped samples from the two distributions were then compared to examine the significance of their difference.

Searchlight RSA. We also performed a 2D surface-based searchlight analysis in order to show the cortical topology of the RE-AN and RE-AI similarity values. For each vertex, the same 2D searchlight disk was defined as above. We then repeated the same RSA on the brain, producing two cortical maps with respect to the RE-AN and RE-AI similarity values.

Forward encoding modeling. We first trained forward encoding models only based on the RE images data in the brain and the DNN. For the response sequence $\mathbf{y} = \{y_1, \dots, y_d\}^T$ of one vertex to the RE images, it is expressed as Eq. (4):

$$\mathbf{y} = \mathbf{X}\mathbf{w}, \quad (4)$$

\mathbf{X} is an m -by- $(n+1)$ matrix, where m is the number of training images, and n is the number of features in a DNN layer. The last column of \mathbf{X} is a constant vector with all elements equal to 1. \mathbf{w} is an $(n+1)$ -by-1 unknown weighting matrix to solve. As the number of training samples m was less than the number of features n in all DNN layers, we imposed an additional sparse constraint on the forward encoding models to avoid overfitting:

$$\min_{\mathbf{w}} \|\mathbf{w}\|_0 \quad \text{subject to } \mathbf{y} = \mathbf{X}\mathbf{w}, \quad (5)$$

Sparse coding has been widely suggested and used in both neuroscience and computer vision ([Vinje WE and JL Gallant 2000](#); [Cox DD and RL Savoy 2003](#)). We used the regularized orthogonal matching pursuit (ROMP) method to solve the sparse representation problem. ROMP is a greedy method developed by Needell D and R Vershynin ([Needell D and R Vershynin 2009](#)) for sparse recovery. Features for prediction can be automatically selected to

avoid overfitting. For the selected 400 vertices in each human ROI, we established 8 forward encoding models using features in 8 DNN layers, respectively. This approach yielded a total of 40 forward encoding models ($5 \text{ ROIs} \times 8 \text{ layers}$) for one subject.

We calculated Pearson correlation between the multivariate responses evoked by the adversarial images and predictions from the trained forward encoding models. To test the prediction accuracy against the null hypotheses, we randomized the image labels and performed permutation tests as described above. Error bars (Fig. 6) indicate 95% confidence intervals obtained by bootstrapping across selected vertices in a brain ROI. Specifically, we resampled 80% vertices in a brain ROI 1000 times without replacement and in each sample recalculated the response prediction accuracy, resulting in a bootstrapped accuracy distribution. The upper and lower bounds of the 95% confidence intervals were derived from the bootstrapped distribution. Similarly, we compared the two bootstrapped distributions of prediction accuracy to derive the difference between the RE-AI and RE-AN similarity values.

We also investigated the hierarchical correspondence between the DNN and the human brain. To do so, we calculated which DNN layer (i.e., 1-8) can best explain the responses of each vertex. In each brain ROI, we calculated the proportion of vertices whose responses can be best explained by the units in each DNN layer. We grouped the proportion values of DNN low-level layers (i.e., 1 and 2) and high-level layers (i.e., 7 and 8) across three subjects and two independent trials respectively and performed a paired t-test to examine their difference. To test whether the proportion of vertices corresponding to low-level DNN layers decreased along the brain processing hierarchy (i.e., V1-LO), we separated response in two independent trials and summed up proportion values across layers 1-3 within a subject. A

paired t-test was then performed to examine the proportions of vertices across three subjects and two independent trials between V1 and LO.

RESULTS

RSA reveals dissociable representations of adversarial images in the DNN and the human brain

Previous studies have demonstrated remarkable *similarities* between two systems in neural representations ([Guclu U and MA van Gerven 2015](#); [Cichy RM et al. 2016](#); [Yamins DLK and JJ DiCarlo 2016](#); [Guclu U and MAJ van Gerven 2017](#); [Horikawa T and Y Kamitani 2017](#); [Zhang C et al. 2018](#)). Here we were instead interested in the *differences* of the neural representations with respect to adversarial images. To do so, we first calculated the representational dissimilarity matrix (i.e., 40 x 40 RDM) for each image type in one brain ROI or in one DNN layer. We know that the perceptual similarity between RE and AI images is much higher than the similarity between RE and AN images for human vision, and vice versa for the DNN. But we do not know whether their neural representations follow such behavioral pattern. We thus used the RDMs to quantify the RE-AN similarity—the correlation between RDMs of the RE and AN images, and the RE-AI similarity—the correlation between RDMs of the RE and AI images. Both types of similarity used RE images as the reference such that they indicate how similar the representations of the two types of adversarial images and RE images.

In the human brain, the RE-AI similarity values were significantly higher than baselines in almost all ROIs across three subjects (Fig. 3, permutation test, all p s < 0.005, see

Methods) whereas almost all the RE-AN similarity values were not significantly different from baselines (permutation test, all p s > 0.05 , except the RE-AN similarity (400 vertices) for V4 in subject 3, $p = 0.022$). These results demonstrated that for the human brain the AI images indeed “look” like the RE images in terms of neural processing and the AN images are almost equivalent to randomized noise. More importantly, we found reliable higher RE-AI similarity values than RE-AN similarity values in all ROIs (Fig. 3, bootstrap test, all p s < 0.0001), indicating that the overall neural processing of the AI images was more consistent with the RE images. Notably, such representational regime is also consistent with the human perceptual similarity. In other words, at least on these images stimuli, we found that the neural representation in the human brain follows the outcome visual perception.

We also performed a searchlight analysis on the cortical surface to reveal the cortical organization of the RE-AI difference. The searchlight analysis used the same calculation as above and allowed us to examine the topology of such functional differences along the cortical sheet of the brain. The searchlight analysis replicated the results above (Fig. 4) and demonstrated that the overall RE-AI similarity was higher than the RE-AN similarity in a distributed fashion in early human visual cortex.

By contrast, the representational structure was remarkably different in the DNN. In the DNN, the RE-AI similarity values were higher than baselines across all layers except the output layer (Fig. 5, permutation test, all p s < 0.0). Interestingly, the RE-AN similarity values were initially low ($p > 0.05$ in layers 1-2) but then became higher than baselines in later layers (all p s < 0.05 in layers 3-8 and the output layer). Besides, we found that the RE-AI similarity values were higher than RE-AN similarity values in low-level DNN layers (i.e.,

layers 1-7, bootstrap test, all p s < 0.0001) but not in layer 8 ($p = 0.375$). The AI-AN separation in low-level layers demonstrated that adversarial images, especially the AN images, actually cannot “fool” the DNN in early visual processing. However, the RE-AN similarity increased dramatically from low- to high-level layers (Mann–Kendall test, $p = 0.0012$) and the RE-AI similarity kept relatively stable across most layers in the DNN (Mann–Kendall test, $p = 0.4655$). Notably, the RE-AN similarity exceeded the RE-AI similarity in the output layer ($p = 0.067$). In other words, even though the RE-AI similarity was higher than the RE-AN similarity in almost all DNN layers, the output layer still wrongly classified the image. These results are surprising since previous studies only demonstrated the perceptual consequence of adversarial images (i.e., output from the top layer) and here we demonstrated that the processing error of the AN images accumulated from low- to high-level layers in the DNN. The increase of the RE-AN similarity resulted in almost identical RE-AI and RE-AN similarity values in layer 8 and even higher RE-AN similarity in the output layer. Most importantly, the representational pattern in all DNN layers (except the output layer) is inconsistent with the “percepts” of the DNN, as the DNN can successfully recognize the AN images but not the AI images. In other words, unlike the human brain, we found an astonishing representation-perception disassociation in the DNN.

We speculate that the representation-perception disassociation in the DNN might be due to two differences compared to the human visual system. First, the DNN can only recognize the AN but not the AI images even though the RE-AI and the RE-AN similarity values were comparable in the top layer. This finding implies that the readout or decision mechanism in the DNN might be suboptimal given the inconsistency between the

representation in the output layer and the representations in previous layers. We speculate the reason is that the DNN classifies the input image as the category with the highest posterior probability. This is essentially a point-estimation without considering the full uncertainty distribution. The classification probability for the true category might be also very high albeit lower than the highest probability. By contrast, numerous studies in human vision have shown that visual processing in humans not only computes the maximum posterior probability to form perceptual choices but also takes into account the uncertainty of the choice ([Ernst MO and MS Banks 2002](#); [Knill DC and A Pouget 2004](#)). Second, given the feedforward structure, all perceptual outcomes of the DNN can only rely on the representation in the top layer. Thus, although the representation in early layers can distinguish two types of images, the decision layer of the DNN cannot directly readout information from early layers. The human visual system, however, consists of densely interconnected brain areas and it has been known that decision mechanisms in human vision are highly flexible ([Heekeren HR et al. 2008](#); [Gold JJ and AA Stocker 2017](#)). Such flexible decision mechanisms support flexible visual behavior when humans are confronted with the ever-changing external environment. We will further address these issues in the discussion section.

Forward encoding modeling bridges responses in the DNN and human visual cortex

RSA mainly focuses on the comparisons between different types of images within one visual system, but it does not directly link the representation in the DNN and the human brain. We next explored an alternative approach—forward encoding modeling—to directly bridge

representations between the two systems. In brief, forward encoding models assume that the activity of one unit in the brain is the linear combination of activity of multiple units in a DNN layer. Using this approach, researchers have previously found that the gradient of complexity of visual features processed in the human ventral pathway can be well predicted by increasingly complex features in the DNN ([Guclu U and MA van Gerven 2015](#); [Guclu U and MAJ van Gerven 2017](#)). However, previous studies only employed RE images, on which both DNNs and human vision can achieve comparable recognition performance. Here instead we used adversarial images and aimed to examine the robustness of such DNN-brain correspondence in the circumstance that identical visual input yields distinct perceptual outcomes in the two systems.

Following previous studies, we first trained forward encoding models only using RE image data. A forward encoding model was established between a pair of brain ROI and DNN layer. Thus we totally obtained 40 (5 ROIs x 8 layers) forward encoding models for one subject. We then examined how well these trained forward encoding models can generalize to the AN and AI images. The rationale is that, if the brain and the DNN process the RE and adversarial images in the similar fashion, the forward encoding models trained on the RE images should transfer to the adversarial images, and vice versa if not. We found that almost all trained encoding models successfully generalized to the AI image data (Fig. 6, warm color bars, permutation test, $p_s < 0.05$ for 113 out of the 120 models for three subjects) but not to the AN image data (Fig. 6, cold color bars, permutation test, $p_s > 0.05$ for 100 out of the 120 models). Moreover, we found that the forward encoding models exhibited much stronger predictive power on the AI images than the AN images (bootstrap test, all $p_s < 0.05$, except

the encoding model based on layer 8 for LO in subject 2, $p = 0.11$). This result demonstrated that the functional correspondence between the two systems as suggested by prior studies only holds when processing RE and AI images but not AN images. This result is also consonant with the RSA above and demonstrated that the processing of the AN images drastically differed from the processing of other two types of images. In other words, both systems treated the RE and the AI images similarly, but the AN images differently. In this aspect, the processing regimes of the two systems are consistent. But again, note that the DNN exhibited the opposite behavioral pattern as human vision.

Hierarchical correspondence between the DNN and human visual cortex only holds for AI images

Previous studies have revealed that the increase of tuning complexity along human ventral stream corresponds to the increase of feature complexity from low- to high-level layers in DNNs ([Guclu U and MA van Gerven 2015](#); [Zhang C et al. 2018](#)). To investigate such hierarchical correspondence in the adversarial images, we examined which DNN layer (i.e., 1-8) could best explain the responses of each vertex. In each brain ROI, we then calculated the proportion of vertices that corresponded to each DNN layer. Since all brain ROIs here are relatively early visual areas, we expected that the forward encoding models using low-level features should better characterize the ROI responses. Indeed, this pattern was observed in the AI images (Fig. 7)—low-level DNN layers could best explain the responses of the majority of vertices (layers 1-2 vs. 7-8, paired t-test, $p < 0.0001$). However, in the AN images, eight DNN layers explained the brain responses almost equally well in all ROIs (layers 1-2 vs. 7-8,

paired t-test, $p = 0.2351$). For example, in the three subjects, layer 1 and layer 8 almost explained an equal proportion of vertices in human V1. This is atypical since we know that human V1 mainly processes low-level visual features. In other words, the hierarchical correspondence between the two systems no longer holds in the AN images. Moreover, we found that from V1 to LO, higher-level DNN layers explained more and more vertices (V1 vs. LO, paired t-test, $p = 0.0004$). This is also expected given the aforementioned DNN-brain hierarchical correspondence. But we did not observe such trend in the AN images (V1 vs. LO, paired t-test, $p = 0.5631$). Taken together, these results demonstrated that the hierarchical correspondence between the DNN and the human brain, as previously proposed, is only valid when processing the RE and the AI images, but not the AN images.

DISCUSSION

The recent surge of research on DNNs has tremendously revolutionized the field of computer vision. Thanks to the remarkable representational power, DNNs have also been proposed as a promising computational framework to model biological vision. Existing studies have shown both qualitative and quantitative similarities between the two visual systems ([Guclu U and MA van Gerven 2015](#); [Cichy RM et al. 2016](#); [Hong H et al. 2016](#); [Guclu U and MAJ van Gerven 2017](#); [Horikawa T and Y Kamitani 2017](#)). However, a considerable number of differences still exist as current DNNs can still only achieve human-level performance in a limited range of visual tasks. We argue that understanding their differences holds the key to further foster research on both artificial intelligence and cognitive neuroscience. Here, we employed the adversarial images that generate drastically different perceptual outcomes in the

two systems and examined the neural representations of the images. RSA revealed that the representation of the AI images, compared to the AN images, were more similar to the representations of the corresponding RE images. This representational similarity pattern was consistent with human percepts (i.e., perceptual similarity) of these images. However, the same consistency was not observed in the DNN and instead we discovered a representation-perception disassociation. Furthermore, we used forward encoding modeling to link unit activity in both systems and found that processing of the RE images and the AI images were quite similar but the processing of the AN images significantly deviated. Overall, these observations provide new evidence for the comparison of the DNN and the human vision, and demonstrate that in some cases (e.g., AN images) two systems can have dramatically different internal representations and behavior. Understanding and overcoming these differences is one important direction of future intelligence research.

Bridging the representations between the DNN and the human brain

As the state-of-the-art DNN models have achieved unprecedented performance or even surpassed humans in many subdomains of visual processing, neuroscientists have been striving to use DNNs to model human vision ([Guclu U and MA van Gerven 2015](#); [Jozwik KM et al. 2016](#); [Yamins DLK and JJ DiCarlo 2016](#); [Guclu U and MAJ van Gerven 2017](#); [Horikawa T and Y Kamitani 2017](#)). Although some computational operations (e.g., convolution, nonlinear activation function) of current DNNs bore strong resemblances to the human visual system, it remains unclear whether their internal representations are quantitatively comparable. Guclu U and MA van Gerven ([Guclu U and MA van Gerven 2015](#))

used the forward encoding modeling approach and found that units' activation along the DNN layers can predict the neural responses along the ventral visual pathway in the brain. Such quantitative relationship suggests that both systems implement a computational architecture that extracts increasingly complex visual features along the processing hierarchy. Such hierarchical functional correspondence has also been found in response dynamics ([Cichy RM et al. 2016](#)). In addition to visual processing, one recent study has reported that DNNs for speech recognition can also predict hierarchical responses in the human auditory system ([Kell AJE et al. 2018](#)). These findings highlight the approach of using DNNs as a modeling framework to understand human perceptual systems, especially for some complex tasks of which previous shallow models are not capable. On the other hand, linking the human brain and DNNs may also in turn guide the design of DNNs. To create a more intelligent DNN, showing behavioral and representational similarities between the two systems is valuable but insufficient. Most previous studies have only focused on their *similarities* and only employed the sensory stimuli that can be easily recognized by both systems. Those studies did not reveal the limit of DNNs thus we argue that understanding the mechanistic *differences* between the two systems will provide more useful insights. This is especially beneficial for engineering purposes given that most DNNs are still significantly worse than humans in many complex tasks such as reasoning and inference.

Adversarial images as a tool to probe functional differences between the DNN and human vision

Despite the enthusiasm in linking DNNs and the human brain, Szegedy C et al.

([Szegedy C et al. 2013](#)) took a sober approach and created adversarial images that can successfully “fool” even the state-of-the-art DNNs. This result is surprising and alarming since this imposes problems on the real-life applications of the artificial visual systems (i.e., adversarial attack) ([Yuan X et al. 2017](#)). Several theories have been proposed to explain the phenomenon of adversarial images ([Akhtar N and A Mian 2018](#)). For example, one possible explanation is that DNNs are forced to behave linearly in high dimensional spaces, rendering them vulnerable to adversarial attacks ([Goodfellow IJ, J Shlens, et al. 2014](#)). Besides, flatness ([Fawzi A et al. 2016](#)) and large local curvature of the decision boundaries ([Moosavi-Dezfooli S-M et al. 2017](#)) as well as low flexibility of the networks ([Fawzi A et al. 2018](#)) are all possible reasons. Szegedy C et al. ([Szegedy C et al. 2013](#)) has suggested that current DNNs are essentially complex nonlinear classifiers and this discriminative approach does not consider the overall data distributions. We will further address this issue in the next section.

In this study we focused on one particular utility of adversarial images—to test the extent and limit of similarities between DNNs and the human brain. We argue that revealing functional differences between DNNs and human vision is where the true value of adversarial images lies. Most previous studies employed the natural images that most DNNs have been trained on and it is thus not surprising that those performance-optimized DNNs also showed similar representations as humans. By contrast, some recent studies have started to examine the performance and representation of DNNs in special experimental conditions, such as manipulation of image noise ([Geirhos R et al. 2018](#)) and distortion ([Dodge S and L Karam 2017](#)). The utility of adversarial images in the present study follows this line of research. The rationale is that if DNNs are similar to humans, they should exhibit the same capability not

only in ordinary circumstances but also in some unnatural cases, such as adversarial images. This approach has been adopted in several recent studies ([Flesch T et al. 2018](#); [Rajalingham R et al. 2018](#)).

Possible caveats of DNNs in the processing of adversarial images

Why the DNN and human vision behave differently on adversarial images, especially on the AN images? The deficiencies of DNNs have been recently summarized in recent criticism ([Akhtar N and A Mian 2018](#); [Marcus G 2018](#)). We want to highlight three of them that are related to the processing of adversarial images.

The most important factor is that the current DNNs are only trained to match the classification labels generated by humans. This approach is essentially a discriminative modeling approach that characterizes $p(\text{class}|\text{image})$ and training produces a classifier in high dimensional feature space. In this discriminative approach, there must exist a set of images that fulfill the classifier but fall distantly from the real distribution of the images of the target class. The AN images are such examples. Humans cannot recognize the AN images because humans do not merely rely on discriminative classifier and instead use the knowledge of the generative process that combines both the likelihood $p(\text{image}|\text{class})$ and prior experience $p(\text{class})$. Understanding the generative process allows us to make an inference to the class given an input image. Humans can therefore immediately realize that the AN images clearly lie out of the normal distribution range and should not belong to any object category. Modeling the generative process is challenging because it requires to formulate the full probabilistic relationships between objects in the external world. Some recent studies have

started to investigate generative deep models, such as variational autoencoders ([Kingma DP and M Welling 2013](#)) and generative adversarial networks ([Goodfellow IJ, J Pouget-Abadie, et al. 2014](#)).

Second, most DNNs operate in a pure feedforward fashion but it has been well known that visual computation in the human brain involves profound feedback and recurrent connections. Numerous studies have shown the critical role of top-down processing in a wide range of visual tasks, including recognition ([Bar M 2003](#); [Ullman S et al. 2016](#)), tracking ([Cavanagh P and GA Alvarez 2005](#)), as well as other cognitive domains, such as memory ([Zanto TP et al. 2011](#)), language comprehension ([Zekveld AA et al. 2006](#)) and decision making ([Fenske MJ et al. 2006](#); [Rahnev D 2017](#)). In our results, the responses in human visual cortex likely reflected the combination of feedforward and feedback effects whereas the activity in a DNN layer only reflected the feedforward input from the earlier layer. It is possible that processing errors accumulate because of no top-down correction, as shown in the increase of the RE-AN similarity in the DNN (Fig. 5).

Third, most DNNs do not explicitly take into account the sensory uncertainty into neural computation. As mentioned above, most DNNs are just trained to match class labels generated by humans. It has been well-established in cognitive neuroscience that the human brain computes the outcome perceptual decision as well as the full probabilistic distribution (i.e., performing inference) over all possible outcomes given a visual input ([Knill DC and A Pouget 2004](#); [Pouget A et al. 2013](#)). In this decision-theoretic framework, a percept is a consequence according to a decision rule applied to the internal posterior distribution ([Maloney LT and H Zhang 2010](#)). This posterior distribution will also be propagated into

downstream decision units and influences other aspects of behavior. Neural implementation of sensory uncertainty has been an active research topic in cognitive neuroscience ([Ma WJ and M Jazayeri 2014](#)). By contrast, most DNNs cannot directly utilize uncertainty information because most benchmark image databases such as ImageNet do not provide uncertainty information. DNNs can only model uncertainty as the distribution $p(\text{class}|\text{image})$ (i.e., the last layer in the DNN). This impedes DNNs to truly understand the real distribution of the images in a high-dimensional feature space.

Concluding remarks

In the present study, we directly compared visual representations in one prototypical DNN and neural responses in the human visual system. Unlike previous studies that mostly used RE images, we employed adversarial images that yield distinct percepts in the two systems. Using RSA and forward encoding modeling, we found that the neural representations of the RE and the AI images were similar in both systems but the AN images were idiosyncratically processed in the DNN. These findings suggest that building generative models may be a future direction in which future DNNs can be improved to chase human cognition.

Acknowledgments

We thank Pinglei Bao, Feitong Yang, Baolin Liu and Huaifu Chen for their invaluable comments on the manuscript. This work was supported by the National Key Research and Development Plan of China under grant 2017YFB1002502, the National Natural Science

Foundation of China (No.61701089), and the Natural Science Foundation of Henan Province of China (No.162300410333).

Competing interests

The authors declare that they have no competing interests.

REFERENCES

- Agrawal P, Stansbury D, Malik J, Gallant JL. 2014. Pixels to Voxels: Modeling Visual Representation in the Human Brain. arXiv preprint. arXiv:1407.5104.
- Akhtar N, Mian A. 2018. Threat of Adversarial Attacks on Deep Learning in Computer Vision: A Survey. IEEE Access. 6:14410-14430.
- Bar M. 2003. A Cortical Mechanism for Triggering Top-Down Facilitation in Visual Object Recognition. J Cognit Neurosci. 15:600-609.
- Cavanagh P, Alvarez GA. 2005. Tracking multiple targets with multifocal attention. Trends Cogn Sci. 9:349-354.
- Chen Y, Namburi P, Elliott LT, Heinzle J, Soon CS, Chee MW, Haynes J-D. 2011. Cortical surface-based searchlight decoding. Neuroimage. 56:582-592.
- Cichy RM, Khosla A, Pantazis D, Torralba A, Oliva A. 2016. Comparison of deep neural networks to spatio-temporal cortical dynamics of human visual object recognition reveals hierarchical correspondence. Sci Rep. 6:27755.
- Cox DD, Savoy RL. 2003. Functional magnetic resonance imaging (fMRI)“brain reading”: detecting and classifying distributed patterns of fMRI activity in human visual cortex. Neuroimage. 19:261-270.
- Deng J, Dong W, Socher R, Li L, Kai L, Li F-F. 2009. ImageNet: A large-scale hierarchical image database, In Proceedings of the IEEE Conference on Computer Vision and Pattern Recognition. pp. 248-255.
- Dodge S, Karam L. 2017. Can the early human visual system compete with Deep Neural Networks?, In Proceedings of the IEEE International Conference on Computer Vision

Workshop. pp. 2798-2804.

Ernst MO, Banks MS. 2002. Humans integrate visual and haptic information in a statistically optimal fashion. *Nature*. 415:429-433.

Fawzi A, Fawzi O, Frossard P. 2018. Analysis of classifiers' robustness to adversarial perturbations. *Mach Learn*. 107:481-508.

Fawzi A, Moosavi-Dezfooli S-M, Frossard P. 2016. Robustness of classifiers: from adversarial to random noise, In *Proceedings of the 30th International Conference on Neural Information Processing Systems*; Barcelona, Spain. pp. 1632-1640.

Fenske MJ, Aminoff E, Gronau N, Bar M. 2006. Chapter 1 Top-down facilitation of visual object recognition: object-based and context-based contributions. In: Martinez-Conde S, Macknik SL, Martinez LM, Alonso JM, Tse PU, editors. *Progress in Brain Research*. Elsevier. p 3-21.

Flesch T, Balaguer J, Dekker R, Nili H, Summerfield C. 2018. Comparing continual task learning in minds and machines. *Proc Natl Acad Sci USA*. 115:10313-10322.

Geirhos R, Temme CRM, Rauber J, Schuett HH, Bethge M, Wichmann FA. 2018. Generalisation in humans and deep neural networks. *arXiv preprint*. arXiv:1808.08750.

Gold JI, Stocker AA. 2017. Visual Decision-Making in an Uncertain and Dynamic World. *Annu Rev Vision Sci*. 3:227-250.

Goodfellow IJ, Pouget-Abadie J, Mirza M, Xu B, Warde-Farley D, Ozair S, Courville A, Bengio Y. 2014. Generative adversarial nets, In *Proceedings of the 27th International Conference on Neural Information Processing Systems*; Montreal, Canada. pp. 2672-2680.

Goodfellow IJ, Shlens J, Szegedy C. 2014. Explaining and Harnessing Adversarial Examples.

arXiv preprint. arXiv:1412.6572.

Guclu U, van Gerven MA. 2015. Deep Neural Networks Reveal a Gradient in the Complexity of Neural Representations across the Ventral Stream. *J Neurosci*. 35:10005-10014.

Guclu U, van Gerven MAJ. 2017. Increasingly complex representations of natural movies across the dorsal stream are shared between subjects. *Neuroimage*. 145:329-336.

Heekeren HR, Marrett S, Ungerleider LG. 2008. The neural systems that mediate human perceptual decision making. *Nat Rev Neurosci*. 9:467-479.

Hong H, Yamins DL, Majaj NJ, DiCarlo JJ. 2016. Explicit information for category-orthogonal object properties increases along the ventral stream. *Nat Neurosci*. 19:613-622.

Horikawa T, Kamitani Y. 2017. Generic decoding of seen and imagined objects using hierarchical visual features. *Nat Commun*. 8:15037.

Jozwik KM, Kriegeskorte N, Mur M. 2016. Visual features as stepping stones toward semantics: Explaining object similarity in IT and perception with non-negative least squares. *Neuropsychologia*. 83:201-226.

Kay KN, Rokem A, Winawer J, Dougherty RF, Wandell BA. 2013. GLMdenoise: a fast, automated technique for denoising task-based fMRI data. *Front Neurosci*. 7:247.

Kell AJE, Yamins DLK, Shook EN, Norman-Haignere SV, McDermott JH. 2018. A Task-Optimized Neural Network Replicates Human Auditory Behavior, Predicts Brain Responses, and Reveals a Cortical Processing Hierarchy. *Neuron*. 98:630-644.

Khaligh-Razavi S-M, Henriksson L, Kay K, Kriegeskorte N. 2017. Fixed versus mixed RSA: Explaining visual representations by fixed and mixed feature sets from shallow and

deep computational models. *J Math Psychol.* 76:184-197.

Kingma DP, Welling M. 2013. Auto-encoding variational bayes. arXiv preprint. arXiv:1312.6114.

Knill DC, Pouget A. 2004. The Bayesian brain: the role of uncertainty in neural coding and computation. *Trends Neurosci.* 27:712-719.

Kriegeskorte N, Kievit RA. 2013. Representational geometry: integrating cognition, computation, and the brain. *Trends Cogn Sci.* 17:401-412.

Kriegeskorte N, Mur M, Ruff DA, Kiani R, Bodurka J, Esteky H, Tanaka K, Bandettini PA. 2008. Matching categorical object representations in inferior temporal cortex of man and monkey. *Neuron.* 60:1126-1141.

Krizhevsky A, Sutskever I, Hinton GE. 2012. Imagenet classification with deep convolutional neural networks, In *Proceedings of the Advances in neural information processing systems.* pp. 1097-1105.

LeCun Y, Bengio Y. 1998. Convolutional networks for images, speech, and time series. In: Michael AA, editor. *The handbook of brain theory and neural networks.* MIT Press. p 255-258.

LeCun Y, Bengio Y, Hinton G. 2015. Deep learning. *Nature.* 521:436-444.

Ma WJ, Jazayeri M. 2014. Neural Coding of Uncertainty and Probability. *Annu Rev Neurosci.* 37:205-220.

Maloney LT, Zhang H. 2010. Decision-theoretic models of visual perception and action. *Vision Res.* 50:2362-2374.

Marcus G. 2018. Deep learning: A critical appraisal. arXiv preprint. arXiv:1801.00631.

Moosavi-Dezfooli S-M, Fawzi A, Fawzi O, Frossard P, Soatto S. 2017. Analysis of universal adversarial perturbations. arXiv preprint. arXiv:1705.09554.

Needell D, Vershynin R. 2009. Uniform Uncertainty Principle and Signal Recovery via Regularized Orthogonal Matching Pursuit. *Found Comput Math*. 9:317-334.

Nguyen A, Yosinski J, Clune J. 2015. Deep neural networks are easily fooled: High confidence predictions for unrecognizable images, In *Proceedings of the IEEE Conference on Computer Vision and Pattern Recognition*. pp. 427-436.

Pouget A, Beck JM, Ma WJ, Latham PE. 2013. Probabilistic brains: knowns and unknowns. *Nat Neurosci*. 16:1170-1178.

Rahnev D. 2017. Top-Down Control of Perceptual Decision Making by the Prefrontal Cortex. *Curr Dir Psychol Sci*. 26:464-469.

Rajalingham R, Issa EB, Bashivan P, Kar K, Schmidt K, DiCarlo JJ. 2018. Large-Scale, High-Resolution Comparison of the Core Visual Object Recognition Behavior of Humans, Monkeys, and State-of-the-Art Deep Artificial Neural Networks. *J Neurosci*. 38:7255-7269.

Szegedy C, Zaremba W, Sutskever I, Bruna J, Erhan D, Goodfellow I, Fergus R. 2013. Intriguing properties of neural networks. arXiv preprint. arXiv:1312.6199.

Ullman S, Assif L, Fetaya E, Harari D. 2016. Atoms of recognition in human and computer vision. *Proc Natl Acad Sci USA*. 113:2744-2749.

Vinje WE, Gallant JL. 2000. Sparse coding and decorrelation in primary visual cortex during natural vision. *Science*. 287:1273-1276.

Yamins DL, Hong H, Cadieu CF, Solomon EA, Seibert D, DiCarlo JJ. 2014. Performance-optimized hierarchical models predict neural responses in higher visual cortex.

Proc Natl Acad Sci USA. 111:8619-8624.

Yamins DLK, DiCarlo JJ. 2016. Using goal-driven deep learning models to understand sensory cortex. *Nat Neurosci.* 19:356-365.

Yuan X, He P, Zhu Q, Bhat RR, Li X. 2017. Adversarial examples: Attacks and defenses for deep learning. *arXiv preprint. arXiv:1712.07107.*

Zanto TP, Rubens MT, Thangavel A, Gazzaley A. 2011. Causal role of the prefrontal cortex in top-down modulation of visual processing and working memory. *Nat Neurosci.* 14:656.

Zekveld AA, Heslenfeld DJ, Festen JM, Schoonhoven R. 2006. Top-down and bottom-up processes in speech comprehension. *NeuroImage.* 32:1826-1836.

Zhang C, Qiao K, Wang L, Tong L, Zeng Y, Yan B. 2018. Constraint-Free Natural Image Reconstruction From fMRI Signals Based on Convolutional Neural Network. *Front Hum Neurosci.* 12:242.

A Regular (RE) images



DNN label: Ibizan hound
Human label: Ibizan hound

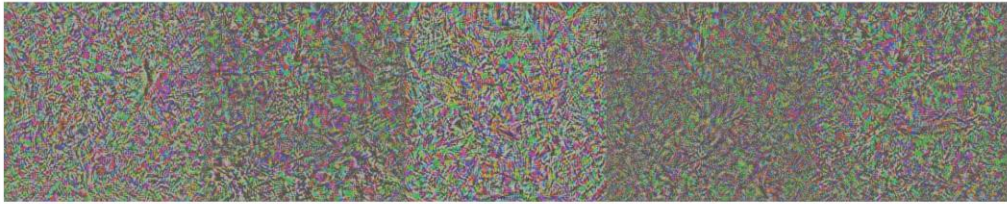
macaw
macaw

police van
police van

banana
banana

garfish
garfish

B Adversarial noise (AN) images



DNN label: Ibizan hound
Human label: noise

macaw
noise

police van
noise

banana
noise

garfish
noise

C Adversarial interference (AI) images



DNN label: sorrel
Human label: Ibizan hound

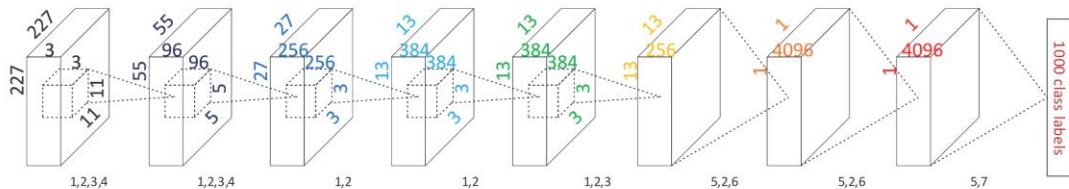
agama
macaw

pool table
police van

ear
banana

chameleon
garfish

D



¹ linear convolution, ² ReLU gating, ³ spatial max-pooling, ⁴ local response normalization, ⁵ inner product, ⁶ dropout, ⁷ softmax

Figure 1. **A-C.** Example regular (RE, panel A), adversarial noise (AN, panel B) images and adversarial interference (AI, panel C) images. The five AN and five AI images one-by-one correspond to the five RE images. The AI images contain a small amount of special image noise but overall look similar to the corresponding RE images. Humans can easily recognize the AI but not the AN images, whereas DNNs can recognize the AN images with over 99% confidence but not the AI images. **D.** AlexNet. Details have been documented in Krizhevsky A et al. ([Krizhevsky A et al. 2012](#)). Each layer uses some or all the following operations: linear convolution, ReLU gating, spatial max-pooling, local response normalization, inner product, dropout and softmax.

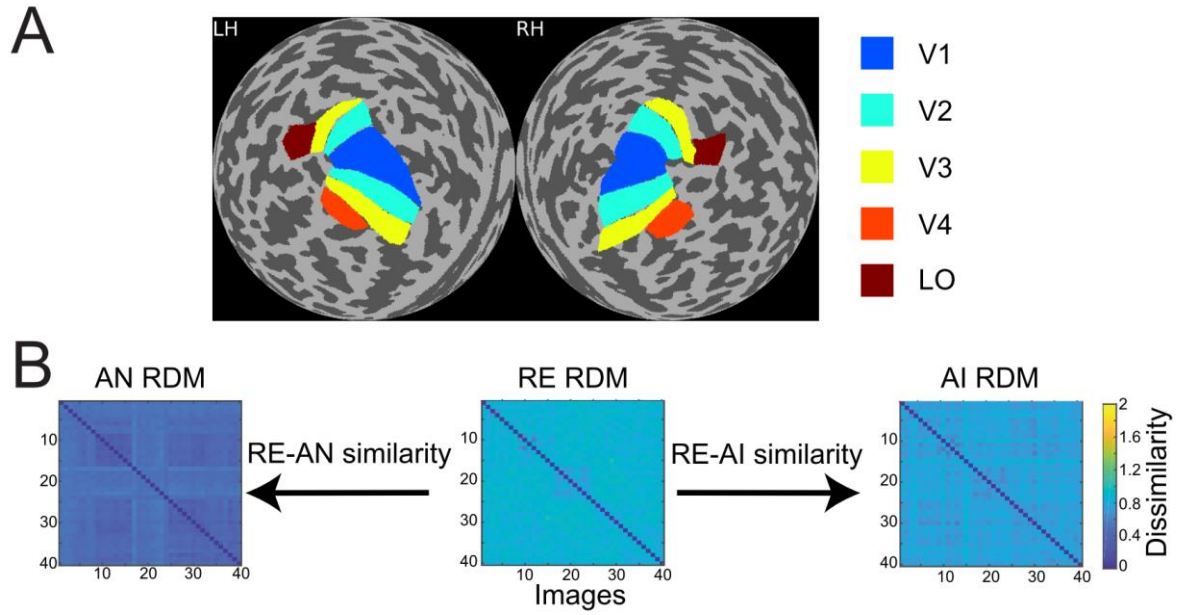


Figure 2. **A.** Regions of interest (ROIs) in a sample subject. Through retinotopic mapping and functional localizer experiments, we identified five ROIs—V1, V2, V3, V4 and lateral occipital (LO) cortex—in both left (LH) and right (RH) hemispheres. **B.** Calculation of the RE-AN and RE-AI similarity values. For each DNN layer, three RDMs are calculated with respect to the RE, AN and AI images. We then calculate the correlation between the AN and RE RDMs, obtaining the RE-AN similarity. Similarly, we can calculate the RE-AI similarity. The same analysis is also performed in each brain ROI.

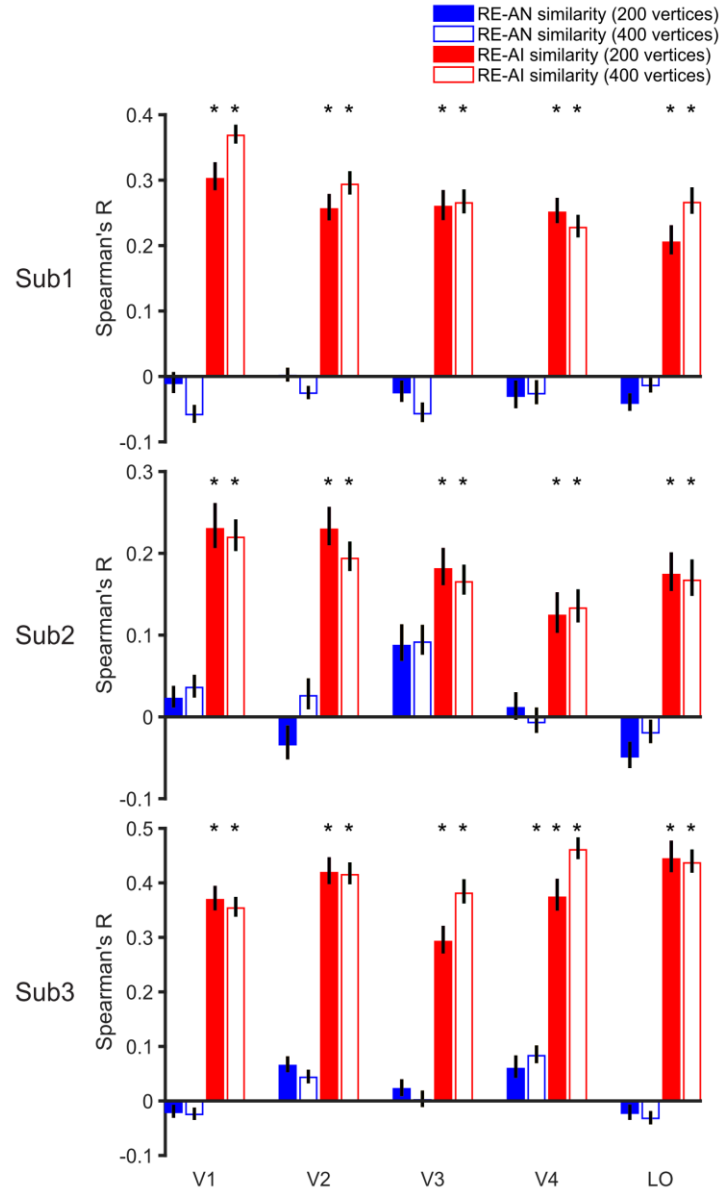


Figure 3. RE-AI and RE-AN similarity in the human brain. Three subplots indicate the three human subjects. The RE-AI similarity indicates the Spearman's R between the RE RDM and the AI RDM in one brain ROI. The RE-AN similarity is calculated in a similar way. The filled and empty bars indicate 200 or 400 vertices selected in each ROI, respectively. In all five brain ROIs, the RE-AI (red bars) similarity values are substantially higher than the RE-AN (blue bars) similarity values, demonstrating that the human visual system processes the AI and the RE images in a similar fashion, but treats the AN images quite differently. This processing regime is also consistent with image perceptual similarity in human vision. Error bars are 95% confidence intervals of similarity values by bootstrapping vertices in one brain ROI. The black asterisks above bars indicate that the similarity values significantly deviate from the null hypotheses (permutation test, $p < 0.05$, see Methods). The same definitions of error bars and significance asterisks are kept in all subsequent images.

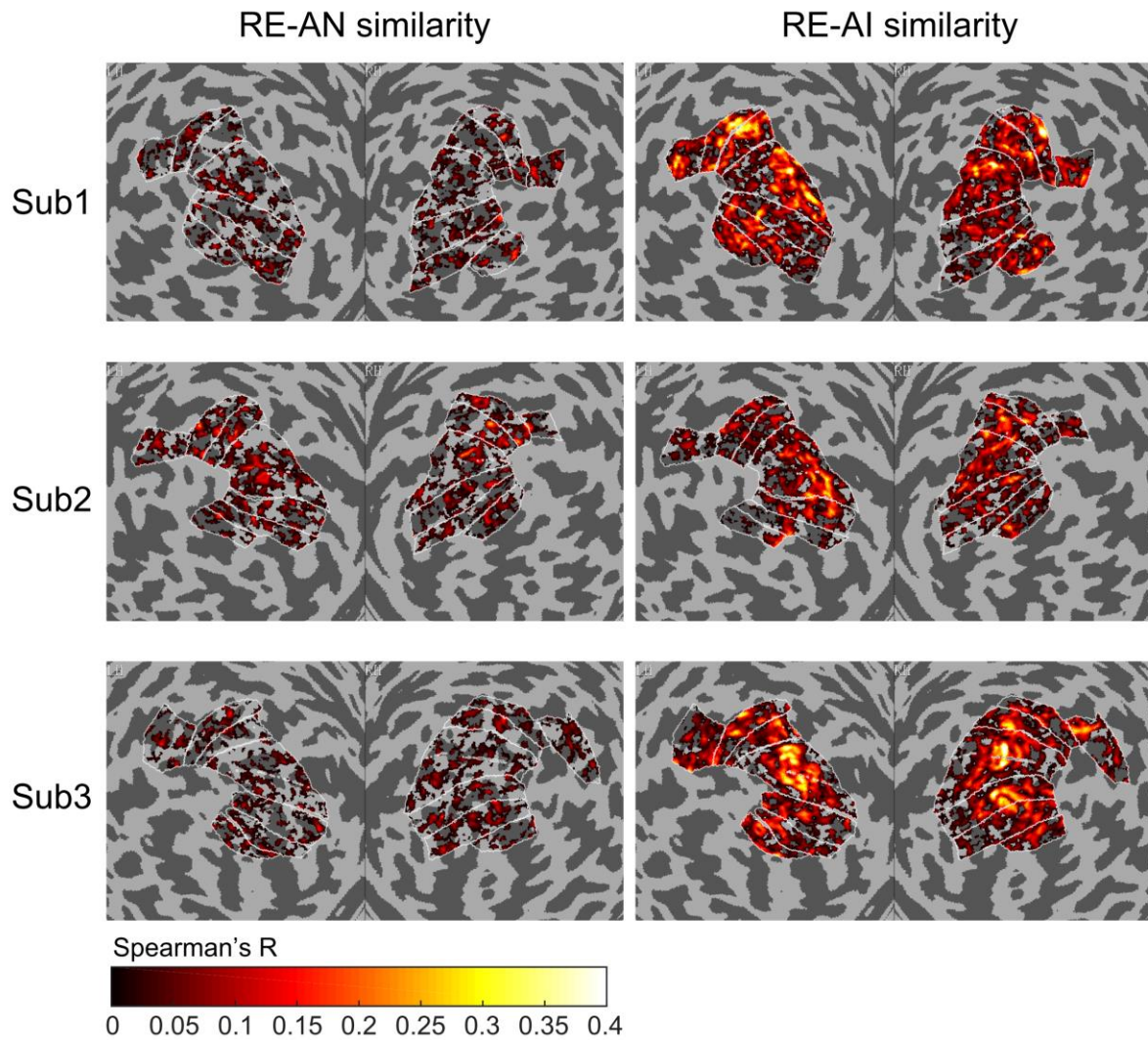


Figure 4. Cortical topology of RE-AI and RE-AN similarity values. The RE-AI similarity is overall higher than the RE-AN similarity across all early visual areas in the human brain.

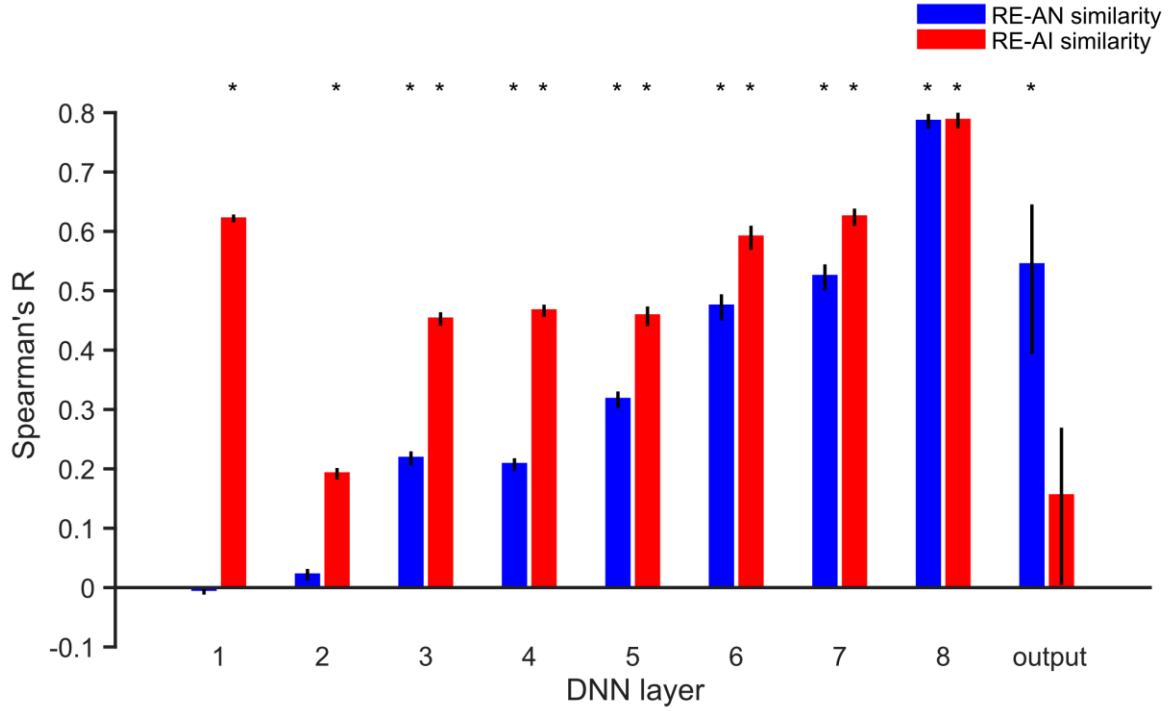


Figure 5. RE-AN and RE-AI similarity values across DNN layers. The same calculation of RE-AN (blue) and RE-AI (red) similarity values was performed using the units' activity in each DNN layer. Note that the output layer contains the probabilities with which the input image belongs to different object categories. The RE-AI similarity values are higher than the RE-AN similarity values in low-level layers. But the RE-AN similarity value increases and the RE-AI similarity value keeps relatively stable along the processing hierarchy. We also see a significant difference between the RE-AN and RE-AI similarity values in the output layer, even though they are quite comparable in layer 8.

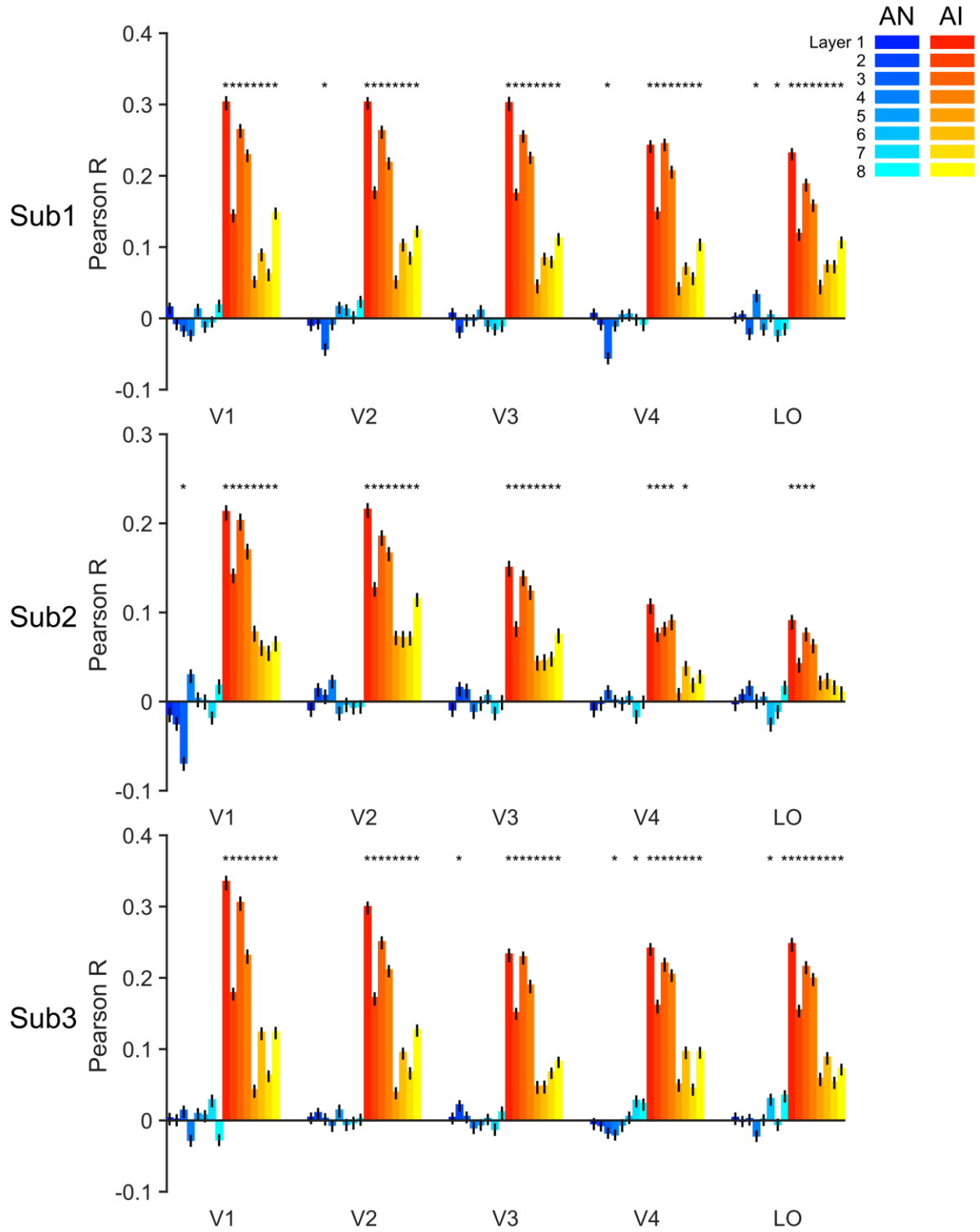


Figure 6. Accuracy of forward encoding models tested on the AN and AI images. The forward encoding models were trained on the responses towards the RE images and then tested on the responses towards the AN and AI images. The transferability of forward encoding models indicates the processing similarity between the RE and AN (cold colors) or AI (warm colors) images.

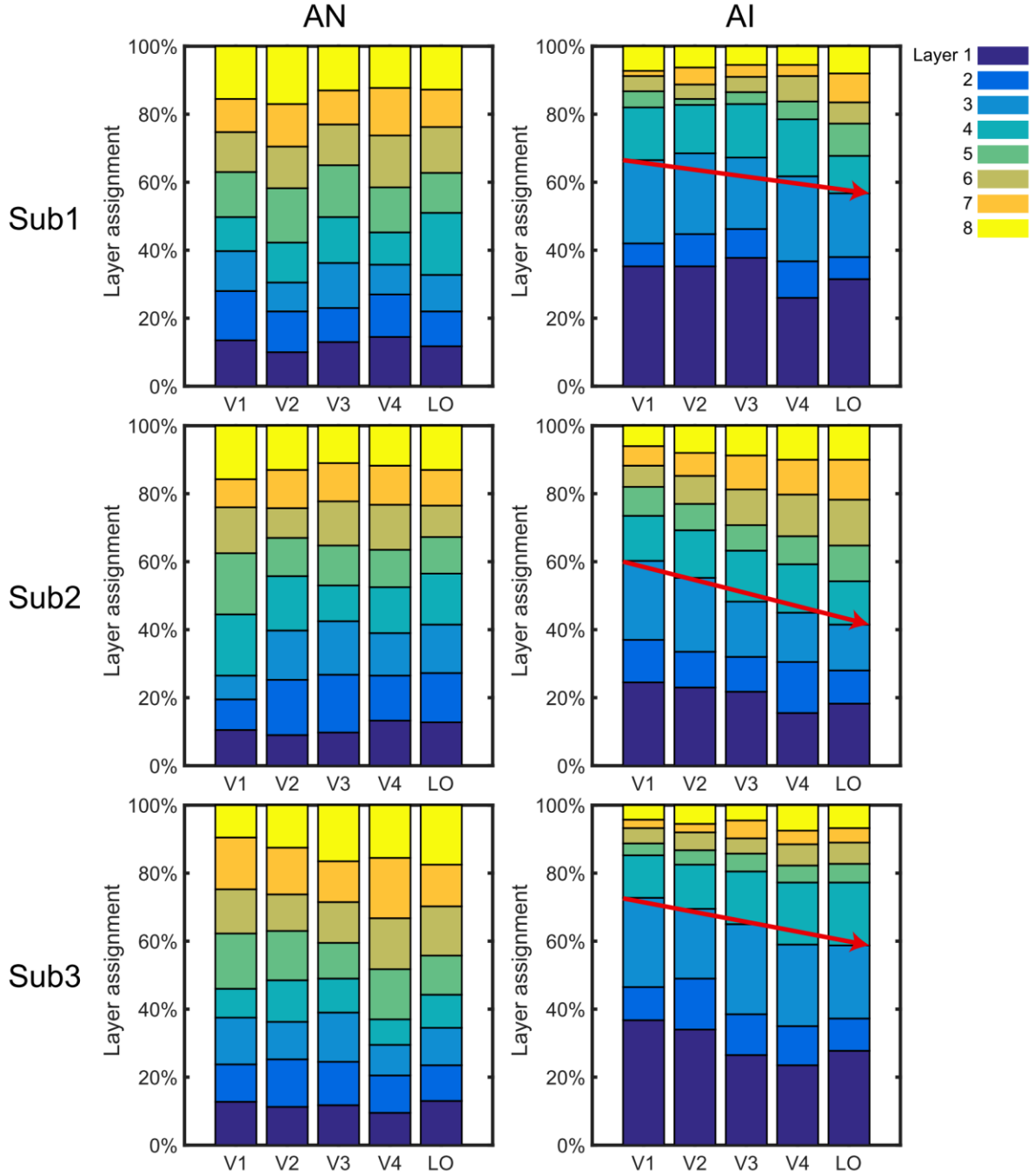


Figure 7. The percentage of vertices that can be best explained by features in each DNN layer. For the AI images, we replicate the hierarchical correspondence between the DNN and the human brain—early visual areas can be better explained by low-level DNN layers. This pattern is, however, not obvious for the AN images. Moreover, the proportion of vertices assigned to high-level DNN layers decreases along processing hierarchy (i.e., V1 to LO) for the AI images (indicated by the red arrows), but not for the AN images. These results indicate that the hierarchical correspondence between the DNN and the human brain only holds for the AI images.